Remotely Detected NMR for the Characterization of Flow and Fast Chromatographic Separations Using Organic Polymer Monoliths

Thomas Z. Teisseyre,[‡,§] Jiri Urban,[†] Nicholas W. Halpern-Manners,[†,§] Stuart D. Chambers,[†] Vikram S. Bajaj,*[,†,§] Frantisek Svec,[∥] and Alexander Pines[†,‡,§]

[†]Department of Chemistry, University of California—Berkeley, Berkeley, California 94720, United States

[‡]Program in Bioengineering, University of California—Berkeley and University of California—San Francisco, California 94133, United States

[§]Material Sciences Division and [∥]The Molecular Foundry, E. O. Lawrence Berkeley National Laboratory, Berkeley, California 94720, United States

ABSTRACT: An application of remotely detected magnetic resonance imaging is demonstrated for the characterization of flow and the detection of fast, small molecule separations within hypercrosslinked polymer monoliths. The hyper-cross-linked monoliths exhibited excellent ruggedness, with a transit time relative standard deviation of less than 2.1%, even after more than 300 column volumes were pumped through at high pressure and flow. Magnetic resonance imaging enabled high-resolution intensity and velocity-encoded images of mobile phase flow through the monolith. The images confirm that the presence of a polymer monolith within the capillary disrupts the parabolic laminar flow profile that is characteristic of mobile phase flow within an open tube. As a result, the mobile phase and analytes are equally distributed in the radial direction throughout the monolith. Also, in-line monitoring of chromatographic separations of small molecules at high flow rates is shown. The coupling of monolithic chromatography columns and NMR provides both real-time peak detection and chemical shift information for small aromatic molecules. These experiments demonstrate the unique power of magnetic resonance, both direct and remote, in studying chromatographic processes.
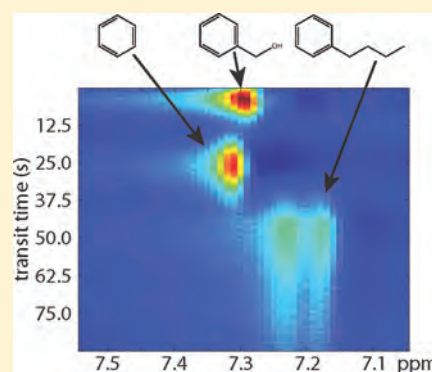
Chromatography is an indispensable tool for the purification and analysis of complex mixtures in many fields, including analytical chemistry, biochemistry, chemical synthesis, drug discovery, and industrial chemical manufacturing.[1] Although UV—visible spectroscopy is the most common method of monitoring chromatographic separations in real-time, it requires well-resolved analyte peaks and the use of chemical standards to correlate species as they elute from the column. Mass spectrometry can also be used for real-time detection, providing an additional method to confirm peak assignments. However, the chemical information provided through mass spectrometry is limited to the mass-to-charge ratio of the individual compounds, unless secondary processes such as fragmentation are utilized. While these secondary processes can yield great insight, they do not provide chemical details of the intact molecules in a noncharged state. Additionally, neither detection method is able to perform multidimensional imaging of flow or separations directly on the column. One powerful alternative to these detection methods is nuclear magnetic resonance (NMR), which has been used for imaging[2−4] and spectroscopy under both stopped[5,6] and continuous flow in-line detection modes.[7,8] In a typical chromatography—NMR experiment, the NMR radio frequency detection coil is positioned at the outlet of a chromatographic column, allowing for continuous monitoring of the effluent. Any columns placed near the magnet must be free of magnetic components, making fused silica capillaries the preferred format. Previous implementations of this concept have been successfully demonstrated for in-line monitoring of microscale separations using particle packed columns.[9−11]

Concurrently, magnetic resonance imaging (MRI) has also been used to image the interior of particle-based chromatographic columns in order to identify flow inefficiencies, to suggest improvements in column design, and to visualize separations as they occur on the columns.[2−4,12] Although insightful, these studies remain limited due to the low sensitivity and poor temporal resolution of MRI. These restrictions preclude its application to the analysis of microscale flow, such as that exhibited in capillary liquid chromatography[13] or on-chip chromatography.[14] In order to analyze separations and flow properties within microscale chromatographic devices, changes need to be made to the detection scheme.

In previous MRI studies of chromatographic columns, the entire column is placed in a single, large radio frequency coil.[2−4,15,16] In this geometry, the fraction of the detector coil volume that is filled by liquid molecules which give rise to the detectable NMR signal is exceedingly small. As the sensitivity of detection is
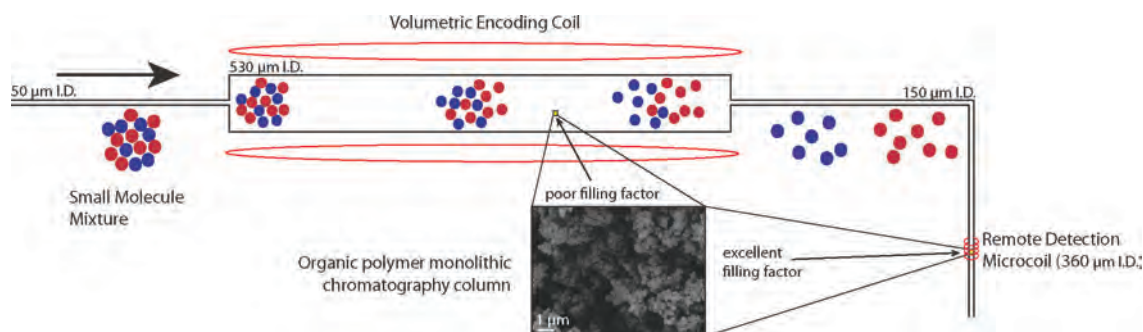
Figure 1. Illustration of the remote detection experiment, as applied to an organic polymer monolithic column. The encoding coil, indicated on both sides of the column, encloses the entire volume of the monolith. The microsolenoid detector is placed at the outlet of the column and provides a sensitivity increase due to the greatly enhanced filling factor for a given voxel.

directly proportional to the filling factor of the coil (the fraction of the coil volume occupied by the sample), a microsolenoid with diameter comparable to the inaccessible microporous features of the column will afford the highest sensitivity.[7,17] In other words, one way to improve sensitivity would be to wind a micro-coil around a specific region of interest inside of the column. While conceptually sound, this is clearly infeasible. As an alternative, remotely detected MRI provides an improved filling factor by separating and optimizing the three stages of the NMR experiment. This remote detection (RD) method has a wide range of applications in both spectroscopy (RD-NMR) and imaging (RD-MRI) and has been described extensively in previous literature.[17−22]

In brief, remote detection separates and optimizes the components of a magnetic resonance experiment (polarization, encoding and detection). This is possible because the steps are correlated in both space and time by the flowing fluid, whose spin degrees of freedom act like a magnetic recording tape in which information can be stored, at one time and place, and read out at a later time. The first stage of remote detection, encoding, occurs within a conventional inductive coil that encloses a sample of interest, such as a microfluidic chip or chromatographic column. This coil is used to encode spatial (RD-MRI), chemical (RD-NMR), and velocimetric information in the phase of the nuclear spin magnetization of the fluid. This information is then converted to long-lived longitudinal spin order and transported, with the fluid, to a single, optimized microcoil detector located at the device outflow. Since the volume of this detector is matched to the volume of the microfluidic features of interest (Figure 1), a sensitivity enhancement of 2−3 orders of magnitude may be achieved.[18,19] Fourier transformation of these data will yield any encoded spectroscopic or image data, as well as a correlated time-of-flight parameter that reflects transport of fluid from the encoding region to the detector. Previous studies show that MRI spatial resolutions of $\sim$15 μm[18] and temporal resolutions of less than 1 ms[19] are possible in microfluidic devices. At these scales, remote detection achieves an improvement in acquisition speed of up to 6 orders of magnitude over traditional MRI.[18] However, the longitudinal relaxation time (T_1) of the encoded spins provides one of the fundamental restrictions to the remote detection experiment. For short T_1 nuclei, such as those used in this study, significant signal loss is observed approximately 5 s after encoding. In order to prevent decay of the stored magnetization, relatively fast flow velocity must be used in order to quickly move the fluid from the encoding region to the detector. In spite of this limitation, the previously described gains in spatial

and temporal resolution make this technique very promising for the analysis of capillary chromatographic separations, provided that the required flow rates can be achieved. Additionally, the remote detection setup is inherently equipped with two separate coils, making it an ideal platform for integrated imaging and in-line spectroscopy in continuously flowing systems. The coupling of remote detection techniques with new developments in fast microseparations, such as porous polymer monoliths, provides a powerful analytical method that can give further insight into both separation dynamics and characterization.

Monolithic chromatographic columns have been widely used for separations since their initial development in the early 1990s.[23] Due to their unique pore structure, traditional polymer monoliths display higher permeability than their particle-based counterparts, while still providing similar separation efficiencies for large molecules.[24−27] These characteristics can allow for faster flow rates and, thus, shorter analysis times than with particle columns. Due to their relative ease of preparation, cost effectiveness, and highly connected porous network that allows convective mass transport to dominate, use of polymer monoliths has grown steadily.[28−30] Despite these advantages, and the availability of polymer monoliths for nearly 20 years, a detailed study of the internal flow dynamics of polymer monoliths has not been reported. One potential reason for this could be that, while polymer monoliths are excellent for the separations of large molecules, the rapid and efficient separations of small molecules have traditionally been a challenge. Recently, in situ hypercros-slinking has been developed to increase the surface area of mono-liths, allowing for more efficient chromatographic separations of small molecules in capillary columns.[28,31] Due to their ability to quickly and efficiently separate small analytes while low back pressures are maintained, hypercrosslinked poly(styrene-co-vinylbenzyl chloride-co-divinylbenzene) monolithic columns are suitable for hyphenated experiments such as combined chromatography−RD-NMR.

This study presents developments in both direct and remote detection NMR for the characterization of polymer monoliths in capillary columns. First, RD-MRI is used for imaging and velocimetry of the mobile phase. This illustrates both the advantages of remote detection experiments on monolithic columns as well as the extreme conditions under which micro-imaging can be performed. Direct in-line monitoring of small molecule separations is then carried out under comparable conditions to demonstrate the unique power of magnetic resonance and the advantages of a simultaneous dual coil platform in studying microscale chromatographic processes.

■ EXPERIMENTAL SECTION

Chemicals and Materials. Styrene (99%), vinylbenzyl chloride (mixture of 3- and 4-isomers, 97%), divinylbenzene (80%, technical grade), 2,2-azobisisobutyronitrile (98%), acetonitrile (HPLC grade), water (HPLC grade), 1,2-dichloroethane, benzyl alcohol, benzene, and butylbenzene were all obtained from Sigma-Aldrich (St. Louis, MO). The monomers (styrene, vinylbenzyl chloride, and divinylbenzene) were purified by passage through a bed of basic alumina to remove the inhibitors. Ferric chloride was purchased from Fisher (New Jersey, NJ). Polyimide-coated 530 μm i.d. fused silica capillaries were purchased from Polymicro Technologies (Phoenix, AZ). The commercial particle packed capillaries (Acclaim phenyl-1, 50 mm × 250 μm i.d., particles 3 μm, average pore size 120 Å) used for ruggedness studies were obtained from Dionex (Sunnyvale, CA).

Preparation of Monolithic Columns. The detailed procedure for the generic monolith preparation has been reported previously.[31] In brief, generic monoliths were prepared in capillaries using in situ polymerization of mixtures of 21% styrene, 7% vinylbenzyl chloride, and 12% divinylbenzene dissolved in binary porogen solvent containing 19% toluene and 41% 1-dodecanol. Azobisisobutyronitrile (1%, w/w, with respect to monomers) was used as the initiator.

The polymerization mixtures were purged with nitrogen for 10 min and then filled into the vinylized capillaries. Both ends of the capillary were sealed with rubber stoppers and the capillary was placed in a water bath. Polymerization was carried out at 70 °C for 20 h. Both ends of the capillary were then cut to adjust its length, and the monolithic column was washed with acetonitrile.

Hypercrosslinking. The monolithic columns were flushed with 1,2-dichloroethane at a flow rate of 0.25 μL/min for 2 h. A filtered solution of 1 g of FeCl$_3$ in 20 mL of 1,2-dichloroethane was pumped through the columns at a flow rate of 0.25 μL/min for 2 h. The hypercrosslinking reaction was then allowed to proceed at 90 °C for 2 h. The modified columns were washed with water overnight and tested.

Liquid Chromatography. LC experiments were performed using an Agilent 1100 system (Agilent, Palo Alto, CA), equipped with a pump, autosampler, and injector. The monolithic capillary column was connected to the injector via an empty 250 cm × 50 μm i.d. connection capillary. The monolith was attached in series with the NMR system described below. Typically, separations were performed in the isocratic reversed-phase mode, using a mixture of 90% acetonitrile (ACN) and 10% water as the mobile phase.

Remote Detection NMR Spectroscopy and MRI. NMR experiments were performed on a 7 T Oxford Instruments (Oxford Instruments, Oxfordshire, UK) superconducting magnet mated to a Varian console (Varian, Palo Alto, CA). The system is equipped with an SGRAD 88/55/HD/S combined shelf-shielded gradient for microimaging and 18 channel room-temperature shim set. For RD-MRI experiments, the monolithic column was centered in a 40 mm Varian volume imaging probe, which served as the encoding coil. The outlet of the column was then connected to the remote microcoil detector by a 5 cm × 150 μm i.d. PEEK capillary (Idex Health & Science, Oak Harbor, WA). The microcoil detector was a 360 μm i.d. 12-turn copper solenoid encased in a cell filled with FC-43 Fluorinert (3M, Maplewood, MN) for susceptibility matching. The column and detection coil were positioned such that both were within the
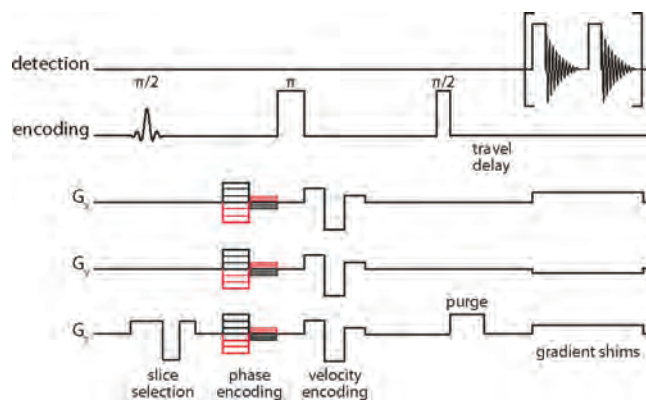

Figure 2. Schematic of the remote detection pulse sequence. The top two lines correspond to RF detection and encoding, respectively. The bottom three lines (G_x, G_y, and G_z) correspond to imaging and velocimetry gradients as well as small gradients applied to tune the static magnetic field homogeneity for detection.

homogeneous region of the magnet. Shimming coils were employed to maximize the homogeneity in the encoding coil. During the microcoil acquisition, the encoding coil-optimized shim values were augmented with precalibrated linear gradients in order to optimize the sweet spot for the detection region. The same microsolenoid was used for both encoding and detection during the small molecule separation experiments. Several papers are available that provide detailed descriptions of the remote detection probe design and experimental setup.[17−22]

Remote Detection MRI of Flow through a Monolith. The mobile phase for these experiments consisted of 100% ACN pumped at a flow rate of 50 μL/min. Details of the procedure for remote detection data acquisition have been described previously.[20] The remote detection NMR pulse sequence is illustrated in Figure 2. Initial excitation consisted of a 5 kHz slice selective pulse, typically a sinc waveform, applied in the presence of a slice selection gradient chosen for region-selective encoding of the column. Following excitation into the transverse plane, phase encoding gradients were applied. The gradient amplitudes were taken as linear combinations of the laboratory-frame gradients, such that the imaging plane was orthogonal to the direction of flow. The phase-encoding gradients were compensated for spin motion up to first order (velocity).[32] The experiment incorporated a spin echo to remove any evolution due to static field inhomogeneities. A final $\pi/2$ pulse was applied to store the encoded information along the longitudinal axis, where phase evolution ceases and the effects of relaxation are greatly diminished. Since the mobile phase was continuously flowing, the encoded information was transported to the volume matched microsolenoid for detection before decay of the stored magnetization. Because the volume of the microsolenoid is smaller than that of the total encoded volume of the column, it can take up to 5 s for encoded fluid to flow through the detection coil. The time-of-flight dimension reflects the flow time between encoding and detection steps in a remotely detected experiment. It is important to note that this differs from the transit (or retention) time described in the directly detected experiments, which references the time between the initial injection and subsequent direct detection in the microsolenoid. The duration of each acquired free induction decay (FID) was correlated to the coil residence time, which was ~80 ms. A total

of 50 time-of-flight acquisitions were collected during the course of remote acquisition.

The entire encoding and detection sequence was repeated for each conjugate-space point of the image. In this case, we acquired 19×19 transverse images with a field of view of $\sim760\ \mu$m and a resolution of $\sim40\ \mu$m.

A position- and acceleration-compensated velocity-encoding gradient was added after the refocusing pulse in order to perform high-resolution velocimetry experiments. Two experiments were performed for each phase encoding point, alternating between positive and negative velocity-encoding gradients to encode displacement in the phase of the spins. The complex phases for the velocity encodes were then subtracted to yield an absolute phase difference image, which was later converted to units of velocity. The strengths of these gradients were chosen to avoid phase wrapping.

For a given volumetric flow rate, the reduced void space in the monolith will lead to higher linear velocities than in the open capillary. Velocity calibrations were performed to match the linear velocities of the monolith and open capillary used for the imaging studies. First, the average linear velocity along the direction of flow was encoded. The encoded volume comprised fluid throughout the entire column, with a flow rate of 50 μL/min. This was done by taking an array of velocity-encoding gradient values and calculating the phase difference between the complementary positive and negative lobes (vide infra). For each gradient value, 50 time-of-flight FIDs were acquired and then inverted to give a spectrum. The phase of the corresponding spectrum resulted in plots of the relative phase at each time-of-flight point. The slope of the linear region of the phase plot is indicative of the flow rate in the column. These plots were averaged across the linear region and over all of the time-of-flight points to give a characteristic phase at the chosen flow rate. Flow rate was varied through the capillary in order to match the average linear velocity with the value calculated for 50 μL/min flow through the column. A match in linear velocities was found between the 50 μL/min volumetric flow rate in the monolith and a 135 μL/min flow rate in the capillary.

Remote Detection Image Processing. RD-MRI acquisitions consisted of 19×19 phase-encoded points, each containing 50 stroboscopically acquired FIDs (80 ms each). These data were analyzed in Matlab (Mathworks; Natick, MA). The individual FIDs were first Fourier transformed, giving a frequency spectrum with peaks for water and acetonitrile. Complex summation was carried out across the ACN peak to yield a single k-space value for each phase encode. Two-dimensional Fourier transformation was then performed across the array of k-space values, resulting in 50 19×19 images, one for each time-of-flight point.

Velocities were determined by taking the phase for each k-space point and subtracting the positive and negative velocity lobe acquisition. To convert from the measured phase difference into the corresponding velocity, one first expands the formula for accrued phase in a series of moments, which correspond to contributions from position, velocity, acceleration, and so on:

$$\varphi(t) = \gamma z_0 \int G(t)\ \mathrm{d}t + \gamma v_0 \int G(t) t\ \mathrm{d}t + \frac{\gamma a_0}{2} \int G(t) t^2\ \mathrm{d}t + \ldots$$

For a velocity-encoding gradient that is compensated for position and acceleration, the only relevant term is the second integral, and we can carry out the appropriate integration across our gradient waveform (which has three lobes: $+G$, $-3/2G$, and $+1/2G$) to
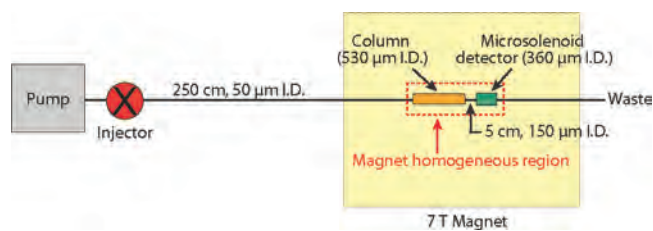

Figure 3. Schematic of the remote detection LC–NMR setup. The pump and injector are connected to the column, inside the 7 T magnet, via a long capillary. Fluid flows through the column, which is enclosed in the encoding volume coil, and into the microsolenoid detector.

arrive at the formula, which converts between phase difference and velocity. In the case of a three-lobe position- and acceleration-compensated gradient with lobe amplitudes as described above, a total duration for all three lobes of τ, and a brief delay between each lobe of α (not counted toward τ), the formula is

$$v = \frac{2\pi\Delta\varphi}{360 G \gamma} \left[\frac{\tau^2}{9} + \frac{\alpha\tau}{3} \right]^{-1}$$

NMR Spectroscopy of Small Molecule Separations. The separation experiments integrated the built-in HPLC injector into the remote detection flow setup, as shown in Figure 3. The separations were carried out at a flow rate of 35 μL/min. The 0.5 μL sample consisted of benzyl alcohol, benzene, and butylbenzene at a ratio of 1:1:7 (1.1:1.3:5.0 M). Upon injection, the spectrometer was triggered to acquire spectra every 250 ms after a preliminary 35 s delay to account for travel through the 250 cm capillary from the injector to the column. Using the autosampler, this sequence was repeated 256 times to increase the signal-to-noise ratio, although an unambiguous view of the separation can be achieved in a single scan, as shown in Figure 6. An extended sequence of 60 injections was also conducted to examine the injection reproducibility

■ RESULTS AND DISCUSSION

Although NMR studies of mobile phase flow dynamics in particle-based columns have been demonstrated,[2,3,16,17] there are no comparable studies of fluid flow within monolithic columns. While both of these column formats enable chromatographic separations, they possess fundamentally different pore structures and may not produce the same flow profile.

A series of two-dimensional remotely detected images in an empty 530 μm i.d. capillary and an organic polymer monolith is shown in Figure 4. These images, which are axial with respect to the direction of flow, show both intensity and velocimetry data. Five of the 50 acquired time-of-flight points are shown, labeled by the time from storage pulse to arrival in the microsolenoid (increasing from left to right). Fluid that is encoded closest to the outlet of the column arrives at the microsolenoid detector first and is therefore detected in earlier times of flight. The progression of images gives a view of the flow profile and dispersion within each system and therefore insight into the overall flow behavior.

The hypercrosslinked monoliths have a reduced interstitial volume compared to the open capillary. As a result, the linear flow velocity within the monolithic column is higher than for the
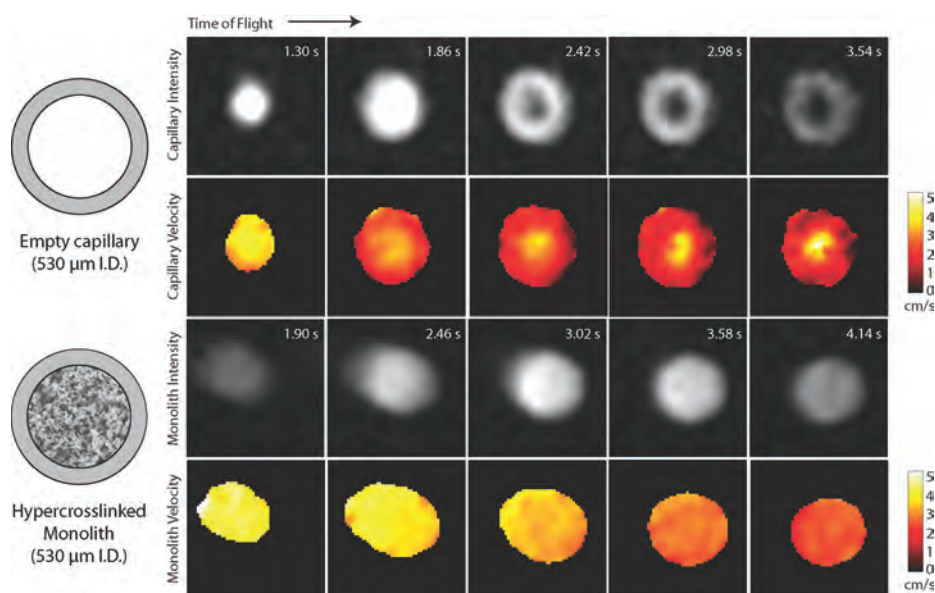
Figure 4. Axial images illustrating intensity and velocity for acetonitrile flowing through the open capillary (top) and monolith (bottom). Five characteristic time-of-flight points were selected and the corresponding images are ordered by their travel time. Conditions: columns, 90 mm × 530 μm i. d.; mobile phase, 100% ACN; capillary flow rate, 135 μL/min; monolith flow rate, 50 μL/min.
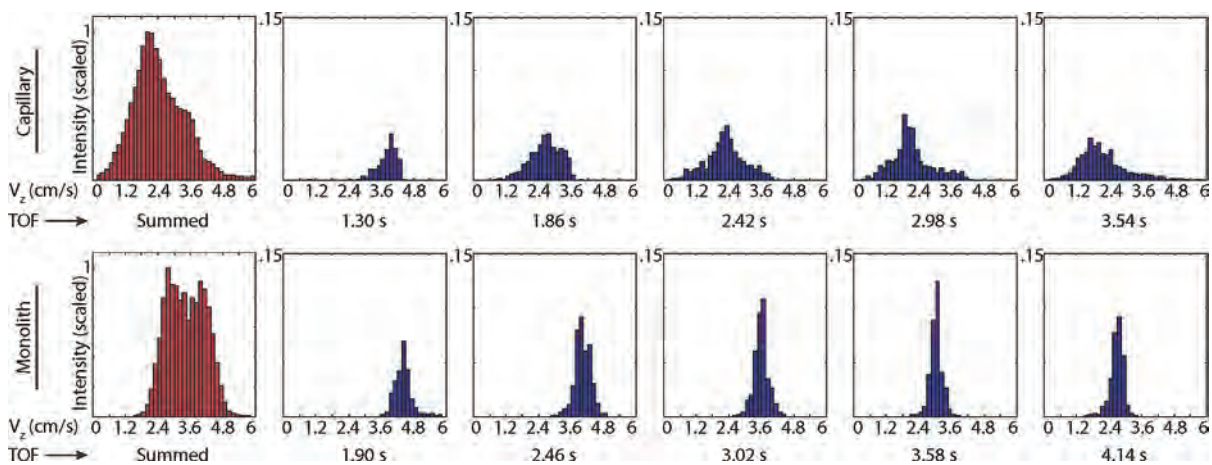

Figure 5. Histograms of the velocity data for both capillary and organic polymer monolith. Summed and individual time-of-flight histograms are shown, corresponding to the same data and conditions found in Figure 4.

empty capillary at the same volumetric flow rate. To provide an equivalent comparison, the volumetric flow rate of the open capillary was increased in order to match the linear velocity to the flow inside of the monolith, as described in the Experimental Section. As would be expected, the first encoded packet of fluid takes longer to arrive in the monolith experiment (1.30 s for the open capillary and 1.90 s for the monolith) since the flow is slower in the capillary connecting the column to the detection region. The time for the entire encoded region to travel through the microsolenoid detector is ~2.25 s in both cases.

Because the flow of the mobile phase is nonturbulent, the early time-of-flight points can be attributed to the liquid, which was closest to the detector at the time of encoding and which therefore arrived at the detector first. This is quantified in the velocity images, which show that fluid in earlier time-of-flight points has higher linear velocities in both the monolith and capillary. The average linear velocities decrease along the time-of-flight

dimension from ~4 cm/s in early time-of-flight points down to ~2 cm/s for later points.

The most significant differences between the two experiments are seen in the flow profile. As expected, a parabolic flow profile is observed in the open capillary, with fluid in the center of the capillary appearing earlier and with higher velocity than fluid near the boundaries. This behavior is characteristic of laminar flow and a no-slip boundary condition. The observed profile is substantially different in the monolith, which has a nearly pluglike profile across the entire radial dimension of the column. These differences illustrate that the unique monolithic pore structure serves to disrupt flow and evenly distribute the mobile phase across the column. It has been demonstrated that the tortuous morphology in monolithic columns can negatively impact the radial distribution of mobile phase across the column.[33] However, it is clearly shown that the monolith instead acts as a continuous natural frit, distributing the mobile phase evenly.

Histograms of the velocity along the direction of flow (Figure 5) can provide quantitative insight into the flow behavior. The histograms are shown for the same time-of-flight points as in Figure 4, as well as for the sum of all time-of-flight points. The individual time-of-flight histograms are scaled to their respective summed histogram, which has its largest bin set to a value of 1. The summed histogram for the empty capillary data shows a clear peak and a significant number of pixels with velocities far from the mean. The additional shoulder seen in this distribution is representative of the large quantity of rapidly moving fluid at the center of the capillary, which retains a noticeably higher velocity than the fluid at the edges (Figure 4). Significantly, the range of velocities observed for the empty capillary is much wider than with the monolithic column, which exhibits a relatively flat distribution of velocities that rapidly drops off on both sides of the histogram. This is consistent with uniform flow across the monolithic column and is unlike the flow within an open capillary, where wall interactions lead to significant drag and a wider velocity distribution. Interestingly, the open capillary shows a maximum velocity that is approximately twice as large as the average, a feature that is characteristic of laminar flow. The individual time-of-flight points show far narrower distributions (and, thus, more uniform velocities) in the monolith, further reinforcing these conclusions. These results are consistent with a relatively uniform flow distribution within the monolith, promoted by homogeneous interactions with the high surface area of the nanoporous material. The enhanced surface area and connectivity within hypercrosslinked organic monoliths are the primary characteristics that lead to the pluglike flow. These same features accommodate fast, efficient separations of small molecules at relatively high concentrations.

Having successfully demonstrated the application of RD-MRI to monolithic columns, investigations into achieving meaningful separations under these unusual flow conditions were performed. As mentioned previously, a rapid flow rate is required to transport the material from the encoding region to the detection coil before the encoded information is lost to relaxation. These conditions run contrary to what is required to produce efficient chromatographic separations, as dictated by the van Deemter curve. Thus, the separation of small molecules using a polymer monolith at high flow rates is a significant accomplishment.

Part of the challenge in monitoring a chromatographic separation with NMR comes from the experimental setup. Most notably, metallic components of the HPLC must be placed at a distance from the superconducting magnet, as they can cause inhomogeneities in the magnetic field and lead to potential physical hazards. As a result, an extended length of empty capillary is required between the HPLC hardware and column, which adds undesirable dispersion to the injection. Additionally, our home-built microsolenoid detector is not fully optimized for sensitivity and requires signal averaging and relatively large injections to achieve adequate signal-to-noise ratio. However, injecting a large volume or a concentrated sample may lead to overloading of the stationary phase.

In spite of these challenges, a fully resolved separation of benzyl alcohol, benzene, and butylbenzene is achieved using a 0.5 μL injection at a high flow rate. A two-dimensional plot showing the aromatic region of the detected NMR spectrum versus the time until detection (indicative of the elution time) is shown in Figure 6. The chemical shift is shown along the horizontal axis and transit time (retention time) along the vertical axis. While signal is observable from these compounds
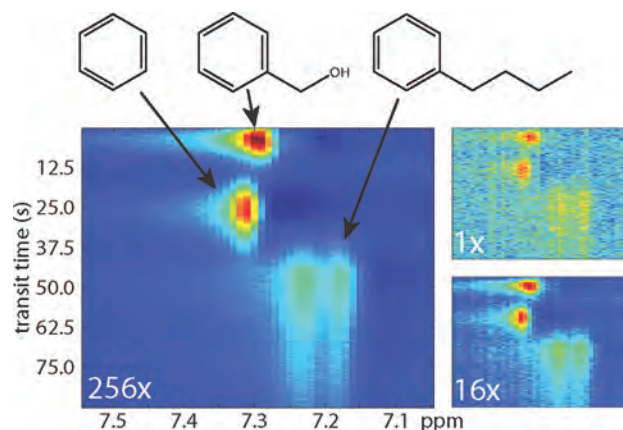

Figure 6. Two-dimensional plot illustrating the separation of benzyl alcohol, benzene, and butylbenzene using a hypercrosslinked monolithic chromatography column. The horizontal axis corresponds to the NMR chemical shift, while the vertical axis represents the transit time of compounds undergoing chromatographic separation determined by the time until detection in the microsolenoid. The data are shown using 1, 16, and 256 signal averages. Conditions: column, 90 mm × 530 μm i.d.; mobile phase, 80−20% ACN and water; flow rate, 40 μL/min; back pressure, 245 bar; sample, benzyl alcohol, benzene, and butylbenzene (1:1:7, 1.1:1.3:5.0 M); injection volume, 0.5 μL.

after a single acquisition, the data shown here are averaged over 16 repeated experiments. By using NMR detection, exact assignment of the eluting compounds can be made based on the chemical shifts of the protons. This is particularly advantageous in situations where multiple components fully or partially coelute, causing overlap in the chromatographic dimension that may still retain distinguishable peaks in the spectral axis. Combining NMR detection with chromatography allows users to observe the identity and quantity of each component as it elutes and is a powerful tool when optimizing conditions for fast, efficient separations. A clear separation is achieved using the model mixture discussed here, where the doublet with the largest upfield shift is characteristic of the butylbenzene protons and the two earlier peaks belong to the benzene and benzyl alcohol protons. Further characterization of the mixture is provided along the transit time dimension, which complements the chemical shift information and allows for optimal identification of compounds.

In addition to their separation capabilities under far from optimal flow conditions, the monolithic columns were found to be very rugged. A series of 60 sequential sample injections (∼300 column volumes) showed less than 2.1% RSD (relative standard deviation) in the travel time from injector to detection coil. This is particularly notable in that the monoliths were subjected to flow rates of greater than 20 μL/min and pressures in excess of 240 bar for several weeks of continuous use. For comparison, two 50 mm × 250 μm i.d. commercial columns packed with 3 μm silica C18 particles were subjected to the same flow and pressure conditions applied to monoliths of comparable dimensions. After only 3 days of use, the particle packed columns showed visible voids at the top, while the monoliths showed no physical signs of degradation. The flexibility and low cost of preparing monoliths in nonmagnetic capillary formats far exceed that of comparable particle-based systems, making them very advantageous for hyphenated NMR techniques.

CONCLUSIONS

Using LC—NMR, a wealth of information can be attained for the characterization of both separations and flow. The additional advantages of remote detection allow information to be encoded within fluids while they are still on the column and provide a tremendous sensitivity enhancement when detecting small volumes of flowing liquid. The requirements of the remote detection are well-suited to the study of hypercrosslinked organic polymer monoliths, which allow for fast flow rates and efficient separations of small molecules. These monoliths are shown to be robust media for the rapid separation of small molecules. Further, in separating the polarization, encoding, and detection steps of an NMR experiment, remote detection enables truly portable LC—NMR instrumentation. Our ongoing work, focusing on the use of portable NMR spectrometers with tailored permanent magnet arrays,[34,35] will obviate the principal restrictions of size and expense.

AUTHOR INFORMATION

Corresponding Author
*E-mail: vsbajaj@lbl.gov.

ACKNOWLEDGMENT

REFERENCES

(1) Snyder, L. R.; Kirkland, J. J.; Dolan, J. W. *Introduction to Modern Liquid Chromatography*, 3rd ed.; Wiley: New York, 2009.

(2) Bayer, E.; Muller, W.; Ilg, M.; Albert, K. *Angew. Chem., Int. Ed. Engl.* **1989**, *28*, 1029–1032.

(3) Dickson, M. L.; Norton, T. T.; Fernandez, E. J. *AIChE J.* **1997**, *43*, 409–418.

(4) Hall, L. D.; Rajanayagam, V. *J. Chem. Soc., Chem. Commun.* **1985**, 499–501.

(5) Tran, B. Q.; Lundanes, E.; Greibrokk, T. *Chromatographia* **2006**, *64*, 1–5.

(6) Limtiaco, J. F. K.; Jones, C. J.; Larive, C. K. *Anal. Chem.* **2009**, *81*, 10116–10123.

(7) Webb, A. G. *Magn. Reson. Chem.* **2005**, *43*, 688–696.

(8) Webb, A. G.; Sweedler, J. V. *Abstr. J. Am. Chem. Soc.* **2002**, *224*, U150–U150.

(9) Grynbaum, M. D.; Kreidler, D.; Rehbein, J.; Purea, A.; Schuler, P.; Schaal, W.; Czesla, H.; Webb, A.; Schurig, V.; Albert, K. *Anal. Chem.* **2007**, *79*, 2708–2713.

(10) Lacey, M. E.; Tan, Z. J.; Webb, A. G.; Sweedler, J. V. *J. Chromatogr. A* **2001**, *922*, 139–149.

(11) Putzbach, K.; Krucker, M.; Grynbaum, M. D.; Hentschel, P.; Webb, A. G.; Albert, K. *J. Pharm. Biomed. Anal.* **2005**, *38*, 910–917.

(12) Zhang, X.; Webb, A. G. *Anal. Chem.* **2005**, *77*, 1338–1344.

(13) Vissers, J. P. C. *J. Chromatogr. A* **1999**, *856*, 117–143.

(14) Lazar, I. M.; Trisiripisal, P.; Sarvaiya, H. A. *Anal. Chem.* **2006**, *78*, 5513–5524.

(15) Tallarek, U.; Baumeister, E.; Albert, K.; Bayer, E.; Guichon, G. *J. Chromatogr. A* **1995**, *696*, 1–18.

(16) Tallarek, U.; Bayer, E.; Van Dusschoten, D.; Scheenen, T.; Van As, H.; Guichon, G.; Neue, U. D. *AIChE J.* **1998**, *44*, 1962–1975.

(17) Seeley, J. A.; Granwehr, J. *J. Magn. Reson.* **2006**, *179*, 280–289.

(18) Bajaj, V. S.; Paulsen, J.; Harel, E.; Pines, A. *Science* **2010**, *330*, 1078–1081.

(19) Harel, E.; Pines, A. *J. Magn. Reson.* **2008**, *193*, 199–206.

(20) Hilty, C.; McDonnell, E. E.; Granwehr, J.; Pierce, K. L.; Han, S.-I.; Pines, A. *Proc. Natl. Acad. Sci. U. S. A.* **2005**, *102*, 14960–14963.

(21) Granwehr, J.; Harel, E.; Han, S.; Garcia, S.; Pines, A.; Sen, P. N.; Song, Y. Q. *Phys. Rev. Lett.* **2005**, *95*, 0755031–0755034.

(22) Moulé, A. J.; Spence, M. M.; Han, S.-I.; Seeley, J. A.; Pierce, K. L.; Saxena, S.; Pines, A. *Proc. Natl. Acad. Sci. U. S. A.* **2003**, *100*, 9122–9127.

(23) Svec, F.; Fréchet, J. M. J. *Anal. Chem.* **1992**, *64*, 820–822.

(24) Premstaller, A.; Oberacher, H.; Huber, C. G. *Anal. Chem.* **2000**, *72*, 4386–4393.

(25) Wang, Q. C.; Svec, F.; Fréchet, J. M. J. *Anal. Chem.* **1993**, *65*, 2243–2248.

(26) Levkin, P. A.; Eeltink, S.; Stratton, T. R.; Brennen, R.; Robotti, K.; Yin, H.; Killeen, K.; Svec, F.; Fréchet, J. M. J. *J. Chromatogr. A* **2008**, *1200*, 55–61.

(27) Hilder, E. F.; Svec, F.; Fréchet, J. M. J. *Anal. Chem.* **2004**, *76*, 3887–3892.

(28) Urban, J.; Svec, F.; Fréchet, J. M. J. *Anal. Chem.* **2010**, *82*, 1621–1623.

(29) Krenkova, J.; Svec, F. *J. Sep. Sci.* **2009**, *32*, 706–718.

(30) Kucerova, Z.; Szumski, M.; Buszewski, B.; Jandera, P. *J. Sep. Sci.* **2007**, *30*, 3018–3026.

(31) Urban, J.; Svec, F.; Fréchet, J. M. J. *J. Chromatogr. A* **2010**, *1217*, 8212–8221.

(32) Pope, J. M.; Yao, S. *Magn. Reson. Imaging* **1993**, *11*, 585–591.

(33) Guiochon, G. *J. Chromatogr. A* **2007**, *1168*, 101–168.

(34) Danieli, E.; Perlo, J.; Blumich, B.; Casanova, F. *Angew. Chem., Int. Ed.* **2010**, *49*, 4133–4135.

(35) Gong, Q. X.; Gordji-Nejad, A.; Blumich, B.; Appelt, S. *Anal. Chem.* **2010**, *82*, 7078–7082.

6010

dx.doi.org/10.1021/ac2010108 |*Anal. Chem.* 2011, 83, 6004–6010